MIMICAD TECHNICAL REPORT NO. 17

Experimentally Verifiable Modeling of Coplanar Waveguide Discontinuities

by

Vesna Radisic

MIMICAD Center
Department of Electrical and Computer Engineering
University of Colorado
Boulder, Colorado 80309-0425

May 1993

Radišić, Vesna (M.S., Electrical Engineering)

Experimentally Verifiable Modeling of Coplanar Waveguide Discontinuities

Thesis directed by Assistant Professor Zoya B. Popović

A general technique for obtaining the frequency dependent scattering parameters of coplanar waveguide structures is discussed. The first step of the analysis is an iterative solution for the charge distribution on the electrodes. A calibrated optical sampling technique allows for direct verification of the validity of the quasi-static charge distribution for structures in which the dielectric layers are electrooptic. In cases where the quasi-static solution is valid, it is shown that the full dynamics of the propagation problem can be recovered from an equivalent nonuniform transmission line, the parameters of which can be determined from the phase velocity and impedance distribution defined by the static charge distribution. Additional measurements using an HP8510 Network Analyzer verify the accuracy of the dynamical part of the method on passive CPW circuits fabricated on GaAs.

ACKNOWLEDGEMENTS

Work described in this thesis has been supported by the NSF Industry / University Cooperative Research Center for Microwave/Millimeter Wave Computer Aided Design under the grant number CDR-8722832 and the Office of Naval Research under the grant number ONRN0014-92-J-1190.

I would like to thank Prof. Zoya Popović for her guidance and friendship during the pursuit of my degree. The assistance of Prof. Alan R. Mickelson and Dr. Dag R. Hjelme is greatly appreciated.

Thanks also to my friends and colleagues in the MIMICAD center. Finally, I would like to thank my parents.

CONTENTS

FIGURES

FIGURE

CHAPTER 1

INTRODUCTION

The goal of the presented work in this thesis is to develop a modeling tool for analysis of discontinuities in coplanar waveguide (CPW) circuits. Currently, there is a lack of computer aided design (CAD) tools for CPW circuits, as compared with the tools available for analysis of microstrip circuits. Furthermore, little information is available in the literature on discontinuity models for CPW [1]. Even though there are an increasing number of characterization techniques becoming available [2, 3, 4], most of these are based on full-wave analysis which require large amounts of computer time and memory. Therefore, further development of simple and accurate modeling tools for CPW discontinuities is necessary.

In order to develop a time efficient algorithm we decided to start with the quasi-static approximation. One quasi-static technique for analysis of microstrip circuits is presented in [5]. Quasi-static techniques are valid up to a certain frequency, and this frequency limit depends on the type of the coplanar structure and its geometry. For CPW, the characteristic impedance and effective dielectric constant depend on the ratio of the widths of the inner conductor to the gaps and are almost independent of substrate thickness. Therefore, the transverse dimensions of a CPW can be chosen to be very small compared to the wavelength. The quasi-static analysis of CPW structures should be valid even for very high frequencies (e.g. up to 60 GHz). Although airbridges need

to be included to eliminate the radiating slot mode, CPW offers several advantages over conventional microstrip lines: shunt and series circuit elements can be easily integrated and the processing yield is improved, since no via holes are required. These advantages make CPW well suited for monolithic microwave integrated circuits (MMICs), even though their application to present has been rather limited.

The most common experimental verification of the quasi-static or full wave techniques is based on the use of a network analyzer. However, such measurements can yield only terminal characteristics, giving S-parameters after proper deembedding. Direct electrooptic sampling [6] can provide much more detailed information than network analyzer measurements can alone. Recent advances in electrooptic sampling calibration allow one to obtain accurate 2-D potential distributions on planar microwave circuits [7].

The analysis technique presented in this paper was motivated by the 2-D electrooptic sampling measurements presented in [7]. Since our technique uses the 2-D potential distribution to compute the 2-D charge distribution, direct electrooptic probing seems to be an ideal tool to use as a verification of our analysis. The two-dimensional (2-D) quasi-static charge distribution on the discontinuous transmission line is then transformed into an equivalent nonuniform transmission line. Since the quasi-static current distribution has zero divergence, a unique local coordinate system on the center conductor can be defined from the current field lines and their normals [5]. This defines an orthogonal curvilinear coordinate system of the equivalent transmission line. The transmission line parameters are expressed in terms of the static charge distribution. Propagation along the equivalent transmission line, therefore, recovers

the full dynamics of the scattering problem from the static charge distribution. This technique is faster than full-wave techniques, because the charge distribution is calculated only once and the time needed to calculate S-parameters for each frequency point is negligible compared to the time needed to calculate the charge distribution. For sufficiently small line dimensions compared to the wavelength, the accuracy of the quasi-static technique should rival that of the full-wave techniques.

In problems involving waveguiding structures, there are two natural length scales: the wavelength of the propagating mode and the size of the waveguide. The size of the waveguide and the discontinuity is generally much smaller than the wavelength of the propagating mode. This leads to a situation in which the fields can be well described by a static field analysis, which is proven by expanding the fields in multiple scale expansion. Our analysis starts from an assumed or measured 2-D potential distribution on the center conductor and the ground planes of the circuit. Using a static Green's function, the surface charge distribution is found from this potential. The corresponding capacitance is then calculated by integrating the charge distribution over the surface of the inner conductor. For any guiding structure that can be considered as a transmission line, knowledge of either the capacitance or inductance is sufficient for computing all line parameters.

CHAPTER 2

THE QUASI-STATIC APPROXIMATION

The modeling of CPW discontinuities in this thesis is based on a quasi-static analysis. This chapter presents a derivation of the conditions under which the quasi-static analysis is accurate, as well as derivation of the analytic algorithm that is implemented in the FORTRAN program.

2.1 A Multiple Scale Expansion

The field solution to the discontinuity scattering problem possesses two scales. Near the discontinuity, the fields vary rapidly on a scale w, where w is the largest transverse dimension of the connecting lines, and then vary slowly with an $O(\lambda_{eff})$ scale, where λ_{eff} is the effective wavelength on the transmission line. The presence of multiple scales can be used to derive an accurate approximations to the full wave problem [8]. To perform a multiple scale expansion of Maxwell's equations we introduce two scaled coordinates

$$\vec{r'} = \vec{r}/w \tag{2.1}$$

$$\vec{r''} = \vec{r}k \tag{2.2}$$

where $k = 2\pi/\lambda_{eff}$. Introducing an expansion parameter

$$\alpha = kw \tag{2.3}$$

we can expand the electric field as [8]

$$E(r) = E^{(0)}(r', r'') + \alpha E^{(1)}(r', r'') + \alpha^2 E^{(2)}(r', r'') + \ldots\ldots \tag{2.4}$$

A similar expansion is used for the magnetic field. The del-operator can be written as

$$\nabla = \frac{k}{\alpha}[\nabla' + \alpha\nabla''], \tag{2.5}$$

where the primed and double primed operators operate on r' and r'' respectively. Introducing the scaled coordinates and field expansions into Maxwell's equations and collecting orders of α, we obtain a multiple scale expansion of the field equations. The zeroth order terms (α^0) show that $E^{(0)}$ and $H^{(0)}$ satisfy the static Maxwell equations in the coordinate r'.

By introducing a new curvilinear coordinate system defined by the static field lines, and neglecting all longitudinal field components in this coordinate system, the first order terms (α^1) show that $E^{(0)}$ and $H^{(0)}$ satisfy the source free Maxwell equations in the coordinate r''. These equations can be written as

$$\frac{\partial}{\partial u_3}(h_1 E^{(0)}) = i\frac{\omega\mu}{k} h_3 h_1 H^{(0)} \tag{2.6}$$

$$\frac{\partial}{\partial u_3}(h_2 H^{(0)}) = i\frac{\omega\epsilon}{k} h_3 h_2 E^{(0)}, \tag{2.7}$$

where h_i are the metric coefficients of the curvilinear coordinate system u_i. The coordinate system is chosen such that $\vec{E}^{(0)}$ is tangential to $\vec{a_1}$ and $\vec{H}^{(0)}$ is tangential to $\vec{a_2}$. u_3 is the coordinate axis normal to the $E^{(0)}$ and $H^{(0)}$ field lines. Equations (2.6) and (2.7) can be transformed to the standard transmission line equations by defining a line voltage as the line integral of $E^{(0)}$ from the center conductor to the ground plane, and a line current as the line integral of $H^{(0)}$ around the center conductor:

$$V(u_3) = \int_1^2 du_1 h_1 E^{(0)} \tag{2.8}$$

$$I(u_3) = \int_{C_1} du_2 h_2 H^{(0)}. \tag{2.9}$$

The capacitance C and inductance L per unit length can be computed from the static fields as well.

2.2 The Quasi-TEM Approximation

By neglecting the longitudinal field components, we have used the same approximation as in the quasi-static approximation of transmission lines with nonuniform dielectric constant. As suggested by our multiple scale expansion, and as has been shown for uniform transmission lines [9, 10], for low enough frequencies of operation, the u_3 components of E and H fields are small enough to be neglected. A "low enough frequency" is defined as a frequency that produces a wavelength large compared to the transverse dimensions of the structure, i.e., a small α parameter. We are considering a CPW structure, for which the inner conductor and the gap width do not exceed $200\,\mu$m. Since GaAs has a dielectric constant of about 13, and we are working with impedances of about $50\,\Omega$, frequencies up to approximately 40 GHz will not violate the quasi-static approximation. For higher frequency operation, one could decrease the inner conductor and gap width in order to minimize the radiation loss.

The propagation constant and characteristic impedance of quasi-TEM lines can be expressed as

$$\beta = \omega\sqrt{LC} \tag{2.10}$$

$$Z_0 = \sqrt{\frac{L}{C}}. \tag{2.11}$$

Since the phase velocity of a quasi-TEM mode is always given by $v_{ph} = c/\sqrt{\epsilon_{eff}}$, L and C are related by the expression $LC = \mu_0\epsilon_0\epsilon_{eff}$, and therefore the knowledge of one of them is sufficient to determine all line parameters.

Under the quasi-static approximation, an effective dielectric constant is given by $\epsilon_{eff} = \frac{C}{C_0}$, where C is the capacitance per unit length of the structure, and C_0 is the capacitance per unit length of the structure with air replacing all dielectric materials. The propagation constant of the line can then be written as

$$\beta = \frac{\omega}{c}\sqrt{\epsilon_{eff}}, \tag{2.12}$$

where c is the speed of light in vacuum. The characteristic impedance of the line can then be calculated from

$$Z_{TEM}(z) = \frac{\beta}{\omega C(z)}. \tag{2.13}$$

In the previous discussion we assumed quasi-TEM propagation, but it can be shown that the generalized transmission line theory holds for nonTEM propagation as well [11, 12].

2.3 Static Charge Distribution

In the quasi-static approximation, the 2-D potential distribution $V(\mathbf{r})$ is related to the charge distribution $\sigma(\mathbf{r})$ by

$$V(\mathbf{r}) = \int_S G(\mathbf{r}, \mathbf{r}')\sigma(\mathbf{r}')d^2r', \tag{2.14}$$

where $G(\mathbf{r}, \mathbf{r}')$ is the static Green's function for the potential due to a charge on the surface S of a semi-infinite dielectric with dielectric constant ϵ_s.

2.3.1 The Green's Function In order to derive the necessary Green's function, a point charge located in medium 1 was considered, h meters away from a flat boundary of medium 2 and the approach given in [13] was followed. Media 1 and 2 are characterized by relative permittivities 1 and ϵ_s, respectively. In medium 1, the electrostatic potential is due to the point charge

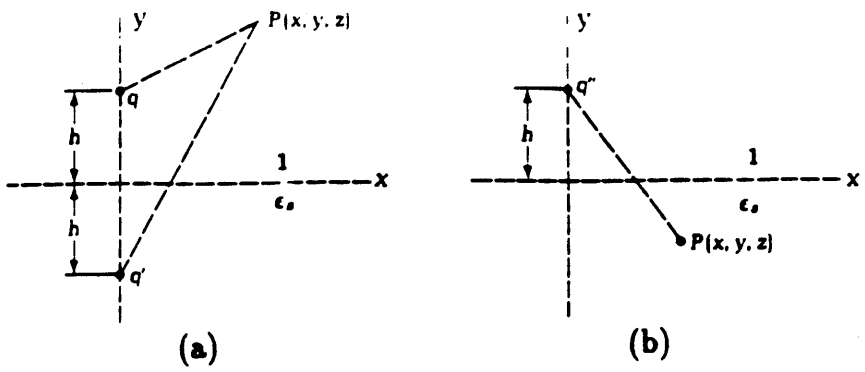

Figure 2.1. (a) To an observer in medium 1, it would appear that there were two charges and (b) to an observer in medium 2 it would appear that there was only one charge located in a homogeneous medium characterized by ϵ_s.

q and its image q', which is located at the mirror-image point of the charge q. The potential in medium 1 may be found as if there were two charges q and q' located in a homogeneous medium characterized by permittivity of 1. The potential in medium 2 is found as if there were a point charge q'' located at the position of the real charge q and as if the whole space were homogeneous and characterized by ϵ_s. This situation is shown in Figure 2.3.1. Values for q' and q'' can be found in terms of q and ϵ_s.

Let us denote $\Phi_1(x,y,z)$ and $\Phi_2(x,y,z)$ as the potential functions in media 1 and 2, respectively. According to the statements given above, the following equations can be set up for $\Phi_1(x,y,z)$ and $\Phi_2(x,y,z)$:

$$\Phi_1(x,y,z) = \frac{1}{4\pi\epsilon_0}\left[\frac{q}{\sqrt{x^2+(y-h)^2+z^2}} + \frac{q'}{\sqrt{x^2+(y+h)^2+z^2}}\right], \tag{2.15}$$

$$\Phi_2(x,y,z) = \frac{1}{4\pi\epsilon_0\epsilon_s}\frac{q''}{\sqrt{x^2+(y-h)^2+z^2}}. \tag{2.16}$$

We require that the following two conditions be satisfied:

$$\Phi_1(x,0,z) = \Phi_2(x,0,z) \tag{2.17}$$

$$\frac{\partial\Phi_1}{\partial y}\Big|_{y=0} = \epsilon_s\frac{\partial\Phi_2}{\partial y}\Big|_{y=0}. \tag{2.18}$$

Applying (2.17) and (2.18) to (2.15) and (2.16), we obtain the equations for q' and q'':

$$q' = q\frac{1-\epsilon_s}{1+\epsilon_s} \tag{2.19}$$

$$q'' = q\frac{2\epsilon_s}{1+\epsilon_s}. \tag{2.20}$$

So, the Green's function for medium 1 is given by:

$$G(\mathbf{r},\mathbf{r}') = \frac{1}{4\pi\epsilon_0}[\frac{1}{\mid \mathbf{r}-\mathbf{r}'-h\mathbf{e_y} \mid} + \frac{1-\epsilon_s}{1+\epsilon_s}\frac{1}{\mid \mathbf{r}-\mathbf{r}'+h\mathbf{e_y} \mid}]. \tag{2.21}$$

In the case where the charges are distributed on the interface, the Green's function is given by:

$$G(\mathbf{r},\mathbf{r}') = \frac{1}{4\pi\epsilon_0\epsilon_{eff}}\frac{1}{\mid \mathbf{r}-\mathbf{r}' \mid}, \tag{2.22}$$

where

$$\epsilon_{eff} = \frac{1}{2}(1+\epsilon_s). \tag{2.23}$$

Equation 2.22 is the one that was used in the program.

A generalized coplanar waveguide discontinuity that we analyzed is shown in Figure 2.2. The total area, S, can be reduced by noting that far away from the discontinuity the charge distribution will remain essentially unperturbed by the presence of the discontinuity. The charge distribution in these areas is assumed to be given by [14]:

$$\sigma(x') = \frac{\epsilon_0(1+\epsilon_s)p}{tK(\sqrt{1+1/p^2})}\frac{1}{\sqrt{(x'^2-1)(x'^2-p^2)}}, \tag{2.24}$$

where $2t$ is the width of the inner conductor, u is the width of the gap and p is given by $p = 1 + u/t$. By dividing the area as shown in Figure 2.2, equation (2.14) can be written

$$V(x,z) = \int_{-L}^{L} dz' \int_{-W}^{W} dx' G(x,x',z,z')\sigma(x',z') + V_{ext}(x,z), \tag{2.25}$$

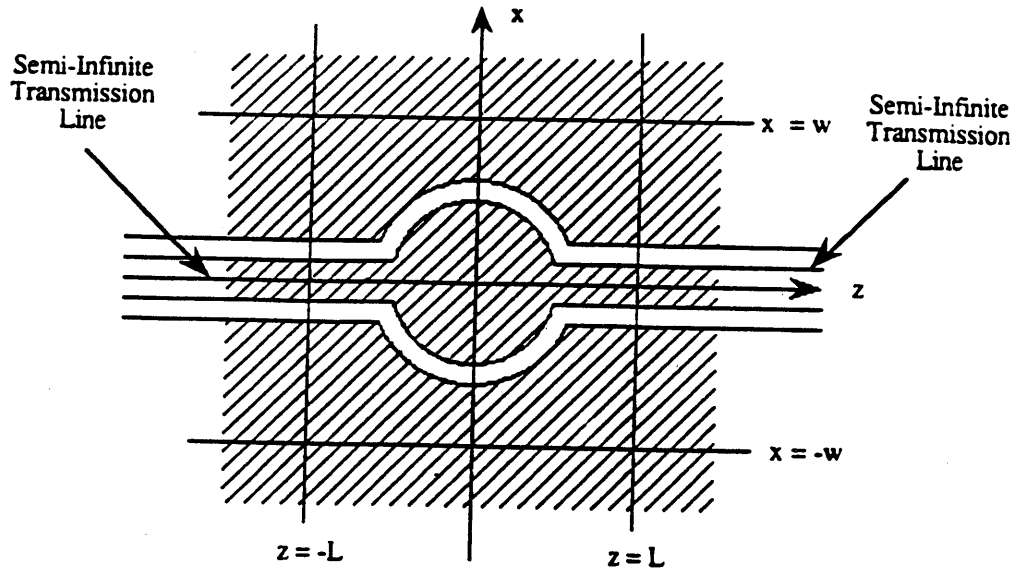

Figure 2.2: A coplanar waveguide discontinuity.

where V_{ext} is the potential in the discontinuity region due to the known charge distribution far away from the discontinuity. $V_{ext}(x,z)$ can be expressed as

$$V_{ext} = V_1 + V_2 + V_3 + V_4, \tag{2.26}$$

where

$$\begin{aligned} V_1 &= \int_{-\infty}^{\infty} dx'\sigma(x') \int_{-\infty}^{-L} dz' G(x',x,z',z) \\ &= \int_{-\infty}^{\infty} dx' G_+(x,x',z)\sigma(x'), \end{aligned} \tag{2.27}$$

$$\begin{aligned} V_2 &= \int_{-\infty}^{\infty} dx'\sigma(x') \int_{L}^{\infty} dz' G(x',x,z',z) \\ &= \int_{-\infty}^{\infty} dx' G_-(x,x',z)\sigma(x'), \end{aligned} \tag{2.28}$$

$$\begin{aligned} V_3 &= \int_{-\infty}^{-W} dx'\sigma(x') \int_{-L}^{L} dz' G(x',x,z',z) \\ &= \int_{-\infty}^{-W} dx' G^W(x,x',z)\sigma(x'), \end{aligned} \tag{2.29}$$

$$V_4 = \int_W^\infty dx'\sigma(x')\int_{-L}^{L} dz' G(x',x,z',z)$$
$$= \int_W^\infty dx' G^W(x,x',z)\sigma(x'), \qquad (2.30)$$

where $\sigma(x)$ is the charge distribution per unit length on the transmission lines away from the discontinuity, and $G_\pm$ and G^W are the Greens functions relating the charge distribution in the exterior region to the potential in the interior region $|z| < L$ and $|x| < W$. These functions are given by

$$G_\pm(x,x',z) = \frac{1}{4\pi\epsilon_0\epsilon_{eff}} \ln \mid (L \pm z) + \sqrt{(L \pm z)^2 + (x-x')^2} \mid^{-1} \qquad (2.31)$$

$$G^W(x,x',z) = \frac{1}{4\pi\epsilon_0\epsilon_{eff}} \ln \frac{\mid (L-z) + \sqrt{(L-z)^2 + (x-x')^2} \mid}{\mid (L+z) + \sqrt{(L+z)^2 + (x-x')^2} \mid}. \qquad (2.32)$$

In writing equations (2.27-2.30) we have assumed that the charge distribution for $\mid z \mid \geq L$ and $\mid x \mid \geq W$ is given by equation (2.24). We can now rewrite equation (2.25) as

$$V_{int}(x,z) = \int_{-L}^{L} dz' \int_{-W}^{W} dx' G(x,x',z,z')\sigma(x',z'), \qquad (2.33)$$

where $V_{int} = V - V_{ext}$ is the actual potential on the conductors minus the potential due to the charges in the exterior region. The solution of the equation (2.33) provides the static charge distribution at the CPW discontinuity. The capacitance per unit length is computed using

$$C(z) = \frac{1}{V} \int_{inner\ cond.} \mid \sigma(x,z) \mid dx, \qquad (2.34)$$

where z is the direction of propagation.

2.4 Numerical Technique

The numerical technique starts with a known value for the voltage distribution (either from theory or from optical sampling measurements).

Then, V_{ext} is found from Equations (2.27-2.30) using numerical integration [15]. Romberg integration is used and two different algorithms are implemented depending on whether the integral is proper or improper. The integral equation (2.33) is reduced to a matrix equation by using point matching [16]. The motivation for doing point matching is the fact that optical sampling measurements give values for the potential at discrete points. Further, in the case where we wish to find the charge distribution from the known voltage distribution on the electrodes, we can always pick known voltages to exist at fixed points. We set

$$V'(\mathbf{r}) = \sum_n v_n \delta(\mathbf{r} - \mathbf{r_n}) \tag{2.35}$$

and expand the charge distribution as

$$\sigma(\mathbf{r}) = \sum_n \sigma_n f(\mathbf{r} - \mathbf{r_n}), \tag{2.36}$$

where $f(\mathbf{r})$ =rect(x/dx)rect(z/dz) and dx and dz define the cell size. The resulting matrix equation takes the form

$$[V] = [G][\sigma], \tag{2.37}$$

where $[\sigma]$ is the unknown vector which contains the solution for the charge density and $[V]$ is the vector which contains the voltages on the electrodes. $[G]$ is the known Green's function matrix with elements

$$G_{n,m} = \begin{cases} G(x_n, x_m, z_n, z_m)dxdz & m \neq n \\ \frac{dxdz}{2\pi\epsilon_0\epsilon_{eff}} \left\{ \frac{1}{dz} \ln(\frac{dz}{dx} + \sqrt{(\frac{dz}{dx})^2 + 1}) + \frac{1}{dx} \ln(\frac{dx}{dz} + \sqrt{(\frac{dx}{dz})^2 + 1}) \right\} & m = n \end{cases} \tag{2.38}$$

Equation (2.38) for the case $n = m$ is derived by solving the integral:

$$\int_{-a}^{a} dx \int_{-b}^{b} dz \frac{1}{\sqrt{x^2 + z^2}} =$$

$$4b \ln[\frac{a}{b} + \sqrt{(\frac{a}{b})^2 + 1}] + 4a \ln[\frac{b}{a} + \sqrt{(\frac{b}{a})^2 + 1}]. \tag{2.39}$$

and by substituting $dx = 2a$, $dz = 2b$ and multiplying by $1/(4\pi\epsilon_0\epsilon_{eff})$.

The unknown 2-D charge distribution can now be found by inverting matrix [G]

$$[\sigma] = [G]^{-1}[V]. \tag{2.40}$$

The matrix inversion can easily be performed using LU decomposition. However, since we are dealing with a 2-D problem, the size of the matrix soon becomes very large (a N x N grid results in a N^2 x N^2 matrix) and large amounts of computer time and storage are needed. The problem at hand seems very well suited for more efficient iteration techniques [15, 17]. The next section gives a short overview of iterative methods that can be used for solving the system of linear equations.

2.5 Iterative Methods for Solving a System of Linear Equations

2.5.1 The Jacobi Algorithm Assume that we are solving the system of linear equations given by Equation (2.37). The Jacobi algorithm gives the solution using the following equations:

$$\sigma_i^{(k)} = \frac{V_i - \sum_{j=1}^{j=i-1} \sigma_j^{(k-1)} G_{i,j} - \sum_{j=i+1}^{N} \sigma_j^{(k-1)} G_{i,j}}{G_{i,i}}, \tag{2.41}$$

where $i = 1, 2, 3, ..$ and $k \geq 1$. If any $G_{i,i} = 0$, reordering equations should be performed so that no $G_{i,i} = 0$. In order to speed up the convergence the equations should be arranged so that $G_{i,i}$ is as large as possible (e.g. using pivoting). A possible stoping criterion is to iterate until:

$$\frac{|| \sigma^{(k)} - \sigma^{(k-1)} ||}{|| \sigma^{(k)} ||} < \varepsilon, \tag{2.42}$$

where $|| \sigma ||$ is a vector norm.

2.5.2 The Gauss-Seidel Algorithm Since, for $i \geq 2$, $\sigma_1^{(k)}$, $\sigma_2^{(k)}$,..., $\sigma_{i-1}^{(k)}$, have already been computed and are supposed to be better approximation, we can use them in equation (2.41):

$$\sigma_i^{(k)} = \frac{V_i - \sum_{j=1}^{j=i-1} \sigma_j^{(k-1)} G_{i,j} - \sum_{j=i+1}^{N} \sigma_j^{(k)} G_{i,j}}{G_{i,i}}. \tag{2.43}$$

Now, we can store only one value for each σ_i instead of two. The Gauss-Seidel algorithm is usually superior to the Jacobi algorithm, but not always.

2.5.3 Relaxation Methods The static charge distribution will often deviate only slightly from a charge distribution composed of 1-D distributions given by equation (2.24). This distribution can be used as the initial value for an iterative technique. In order to solve $[V] = [G][\sigma]$ with a given initial approximation $\sigma^{(0)}$, we used the Gauss-Seidel iterative algorithm with over-relaxation (SOR) [17]

$$\sigma_i^{(k)} = (1 - \Omega)\sigma_i^{(k-1)} + \Omega \frac{V_i - \sum_{j=1}^{j=i-1} \sigma_j^{(k-1)} G_{i,j} - \sum_{j=i+1}^{N} \sigma_j^{(k)} G_{i,j}}{G_{i,i}}, \tag{2.44}$$

where the superscript denotes the iteration number and Ω is a relaxation parameter. If $[G]$ is strictly diagonally dominant, then for any choice of $[\sigma^{(0)}]$ this algorithm gives a sequence $[\sigma^{(k)}]_{k=0}^{\infty}$ that converges to the unique solution of $[G][\sigma] = [V]$ [17]. Over-relaxation parameter values close to 1.5 resulted in rapid convergence for the particular problems considered here. The stopping criterion that was used is given by equation (2.42), where the norm was:

$$|| \sigma || = max_{1 \leq i \leq N} \mid \sigma \mid . \tag{2.45}$$

Since we defined the charge distribution using rectangular functions and defined the voltage across the gap to be unity, the capacitance per unit length is simply

$$C(z) = \sum_{inner\ cond.} \sigma(x_i, z) \tag{2.46}$$

and the TEM impedance follows from equation (2.13).

CHAPTER 3

SCATTERING PARAMETERS

With the quasi-static analysis presented in the previous chapter, we have reduced the problem of propagation in a nonuniform CPW structure to a one dimensional problem of TEM propagation on a continuous nonuniform transmission line. The transmission line equations are easily solved using a number of different techniques. The transmission line network with cascaded sections can be solved using the Riccati equations for S-parameters, or using T-parameters.

3.1 The Riccati Equations

The Riccati equations for the reflection and transmission coefficients are given in [18, 19]. Here, we will use similar equations but for S-parameters. The problem that we are analyzing is shown in Figure 3.1. The S-matrix for a transmission line junction given in Figure 3.2 is given by [20]:

$$[S] = \frac{1}{Z_2 + Z_1} \begin{bmatrix} Z_2 - Z_1 & 2\sqrt{Z_1 Z_2} \\ 2\sqrt{Z_1 Z_2} & Z_2 - Z_1 \end{bmatrix}. \tag{3.1}$$

From equation (3.1) the reflection (designated as ρ further in the text) and transmission (designated as τ) S-parameters can be calculated at a point $z = z_{n-1}$ as:

$$\rho_n = \frac{Z_n - Z_{n-1}}{Z_{n-1} + Z_n} \tag{3.2}$$

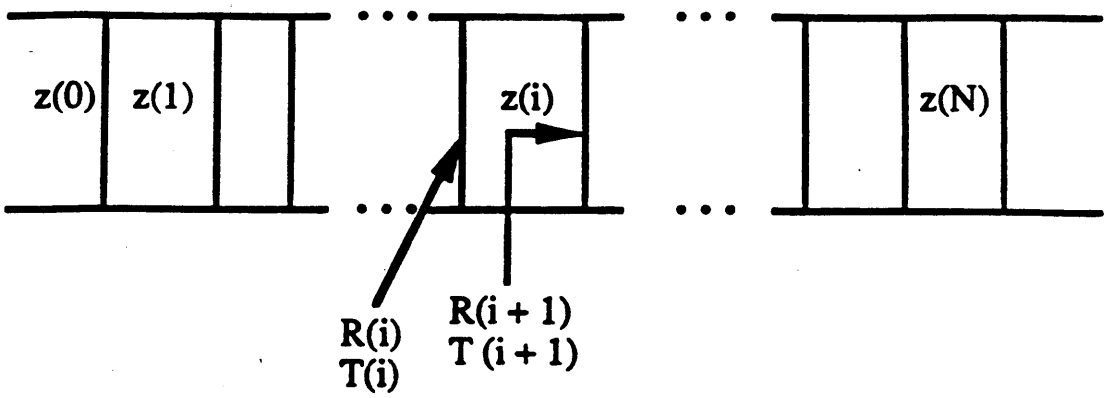

Figure 3.1: General piecewise uniform transmission line.

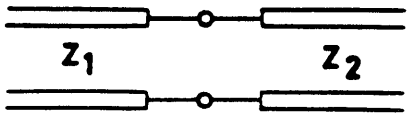

Figure 3.2: A transmission line junction.

$$\tau_n = \frac{2\sqrt{Z_{n-1}Z_n}}{Z_{n-1}+Z_n}, \tag{3.3}$$

where Z_n is the TEM impedance of the line section n. The global S-parameters (S_{11} and S_{21} designated as r and t, respectively) can be found using the following expansion:

$$r_n = \rho_n + \tau_n^2 r_{n+1} e^{j2\beta\Delta} + \tau_n^2 r_{n+1}^2 \rho_n e^{j4\beta\Delta} - \tau_n^2 r_{n+1}^3 \rho_n^2 e^{j6\beta\Delta} + \ldots \tag{3.4}$$

$$r_n = \rho_n + \frac{\tau_n^2 r_{n+1} e^{j2\beta\Delta}}{1+\rho_n r_{n+1} e^{j2\beta\Delta}}, \tag{3.5}$$

then using $\rho_n^2 + \tau_n^2 = 1$ the Riccati equation for the reflection S-parameter can be obtained:

$$r_n = \frac{\rho_n + r_{n+1} e^{j2\beta\Delta}}{1+\rho_n r_{n+1} e^{j2\beta\Delta}}. \tag{3.6}$$

Using similar derivation the Riccati equation for the transmission S-parameter can be obtained:

$$t_n = \frac{\tau_n t_{n-1} e^{j\beta\Delta}}{1 - \rho_n r_{n-1} e^{j2\beta\Delta}}. \tag{3.7}$$

In equations (3.6,3.7), β is given by equation (2.12) and $\Delta = z_n - z_{n-1}$. Regions 0 and $N+1$ are connected to matched loads, so that the initial values are $r_{N+1} = 0$ and $t_0 = 1$. The values for the resulting reflection and transmission S-parameters determine the S_{11} and S_{12}, respectively. Similarly, starting the propagation from the other port, S_{22} and S_{12} can be calculated.

3.2 Transfer Scattering Matrix Representation

If the complete S-matrix is needed, it is perhaps easiest to transform the problem to a transmission line network with N cascaded sections. The scattering matrix representation is not suitable for the analysis of cascaded two-ports. An alternative approach is to convert from S-matrix to ABCD matrix. Another way to analyze the cascaded networks is by using the transfer scattering or T-parameter presentation. T-parameter presentation is preferable to ABCD matrix presentation because of the following considerations. The calculations required for transformation from S-parameters to T-matrix are slightly less complex than those required for S-matrix to ABCD matrix transformation. Also, T-parameters are defined in terms of wave variables normalized with respect to impedances at various ports exactly in the same way as for S-parameters. This allows an easier interchange between the two presentations. The definition of a T matrix and formulae for conversion to S-parameters and vice verse can be found in the literature [20]. The transmission

matrix T_i of the $i-$th section can be written as

$$[T]_i = \frac{1}{\tau_i} \begin{bmatrix} e^{j\beta\Delta} & \rho_i e^{-j\beta\Delta} \\ \rho_i e^{j\beta\Delta} & e^{-j\beta\Delta} \end{bmatrix}. \tag{3.8}$$

The total transmission matrix is then

$$[T] = \prod_i [T]_i. \tag{3.9}$$

Using the transformation relationship between S-parameters and T-parameters:

$$[S] = \frac{1}{T_{22}} \begin{bmatrix} T_{12} & T_{11}T_{22} - T_{12}T_{21} \\ 1 & -T_{21} \end{bmatrix}, \tag{3.10}$$

the complete S-matrix for the CPW structure can be found. The reference planes are kept at the end of the interior region (at $\pm L$), however, they can be shifted by adding the proper phase factors.

CHAPTER 4

THEORETICAL RESULTS

4.1 Application to the Double Step-in-Impedance Discontinuity

The first test structure is a double step-in-impedance, between two $50\,\Omega$ coplanar waveguides, shown in Figure 4.1. The double step was chosen to have $50\,\Omega$ impedance matches at the two ports. Using the procedure outlined in the previous sections, the charge distribution, capacitance per unit length, impedance, reflection and transmission S-parameters along the z coordinate, and the frequency dependent S-parameters for this structure were calculated.

The structure was gridded using rectangular cells with $dx = w_1/11$ and $dz = 2dx$. This resulted in a total of 858 cells on the connecting lines, and 819 cells on the low impedance line. The theoretical static charge distribution was obtained by assuming $V = 1\,\mathrm{V}$ on the center conductor and $V = 0\,\mathrm{V}$ on the ground planes. Figure 4.2 shows the 2-D charge distribution. Charge accumulation at the outer corners of the center conductor and charge depletion at the inner corners are evident. It is this perturbed charge distribution close to the junction that contributed to the discontinuity parasitics. The charge distribution is perturbed over a finite length close to the junctions, resulting in frequency dependent S-parameters.

Figure 4.3 shows the computed capacitance per unit length and impedance

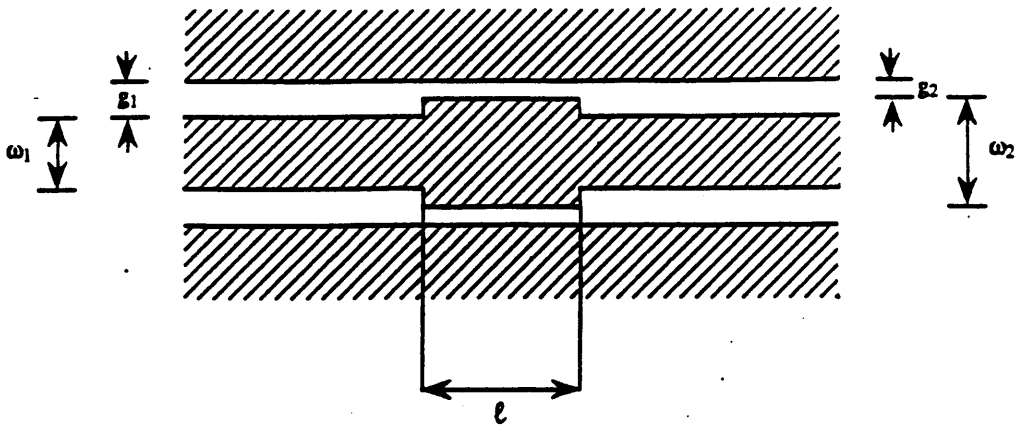

Figure 4.1. A CPW test structure, where $g_1 = 86\,\mu$m, $w_1 = 120\,\mu$m, $g_2 = 46\,\mu$m, $w_2 = 200\,\mu$m and $l = 500\,\mu$m were the dimensions for the fabricated structure.

along the propagation direction. We can compare these results with the characteristic impedance of the CPW line without the discontinuity, using a quasi-static formula from [20]

$$C = \frac{30\pi}{\sqrt{\epsilon_{eff}}} \frac{K(1/p)}{K(\sqrt{1-1/p^2})}, \tag{4.1}$$

where $p = 1 + \frac{2g}{w}$, g is the width of the gap, w is the width of the inner conductor, and K is the complete elliptic integral of the first kind. For the dimensions given in Figure 4.1 the characteristic impedance of the semi-infinite connecting lines is $50\,\Omega$, while for the middle low impedance section it is $36.6\,\Omega$. These are the impedance values from Figure 4.3 far from the discontinuity and at $z = 0$.

The solutions of the Riccati equations are shown in Figure 4.4. The magnitude and phases of r and t along the line are shown for a frequency of $f = 5\,$GHz. The quasi-TEM mode sees a small reflection due to the charge perturbation away from the first junction, and it then experiences a large reflection from the junction. A second large reflection π out of phase is seen at the second junction, nearly cancelling the reflection from the first junction.

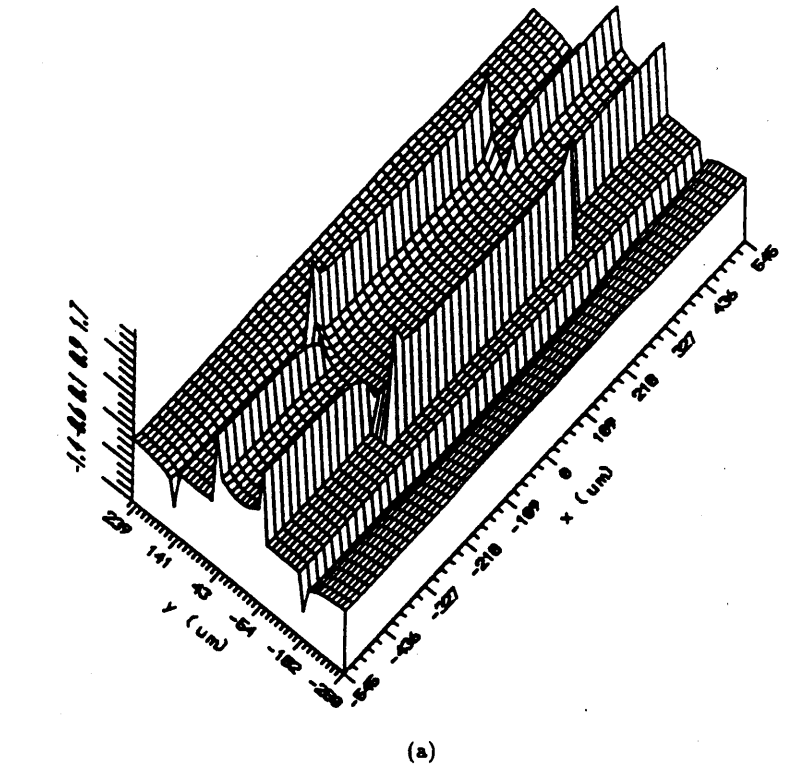

(a)

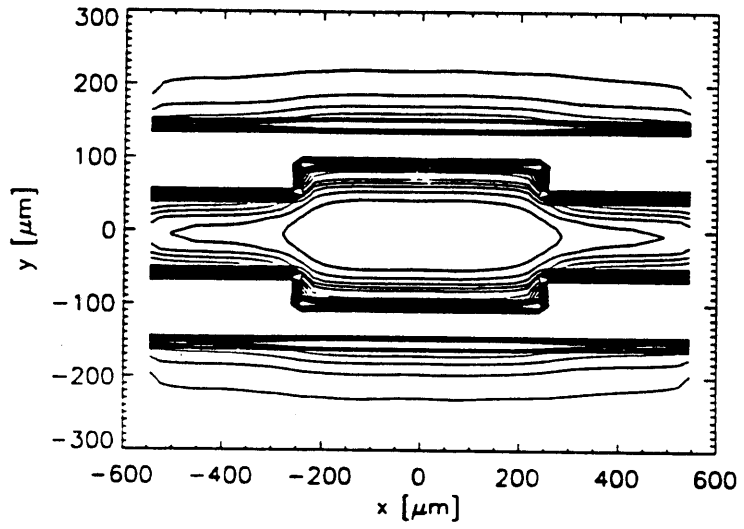

(b)

Figure 4.2: Charge distribution: (a) 2-D and (b) contour plots.

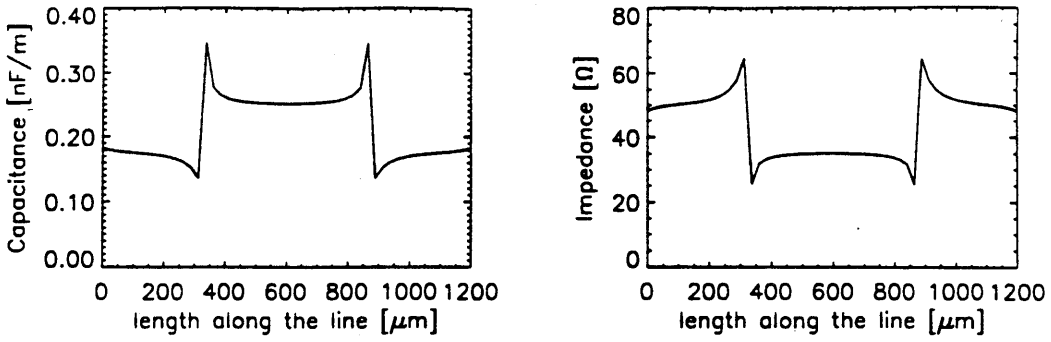

Figure 4.3: Capacitance per unit length and impedance along the line.

While this behavior is expected and rather obvious for this particular discontinuity, the solutions of the Riccati equations can provide useful insight for more complicated geometries.

Figure 4.5 shows the computed magnitudes and phases of S_{11} and S_{21} as a function of frequency. For comparison we have included S_{11} and S_{21} calculated with PMESH, a full wave program developed at the University of Colorado at Boulder [21]. In PMESH, the electrode gaps are gridded instead of the electrodes. We used two cells per cross-section on the input gap and one cell per cross-section on the interior gap. The total number of cells was 42 in the interior part and 136 on the connecting lines. The comparison is quite good for frequencies below 30 GHz. The cause of the large deviations at higher frequencies is not understood at this point. Due to the large number of cells used in our quasi-static analysis, the total computation time for this case was quite long. However, by examining Figure 4.2 (slow variation of σ away from the immediate neighborhood of the junctions) that the number of cells could be drastically reduced without significantly affecting the S-parameter results. Use of symmetry could further reduce the number of cells.

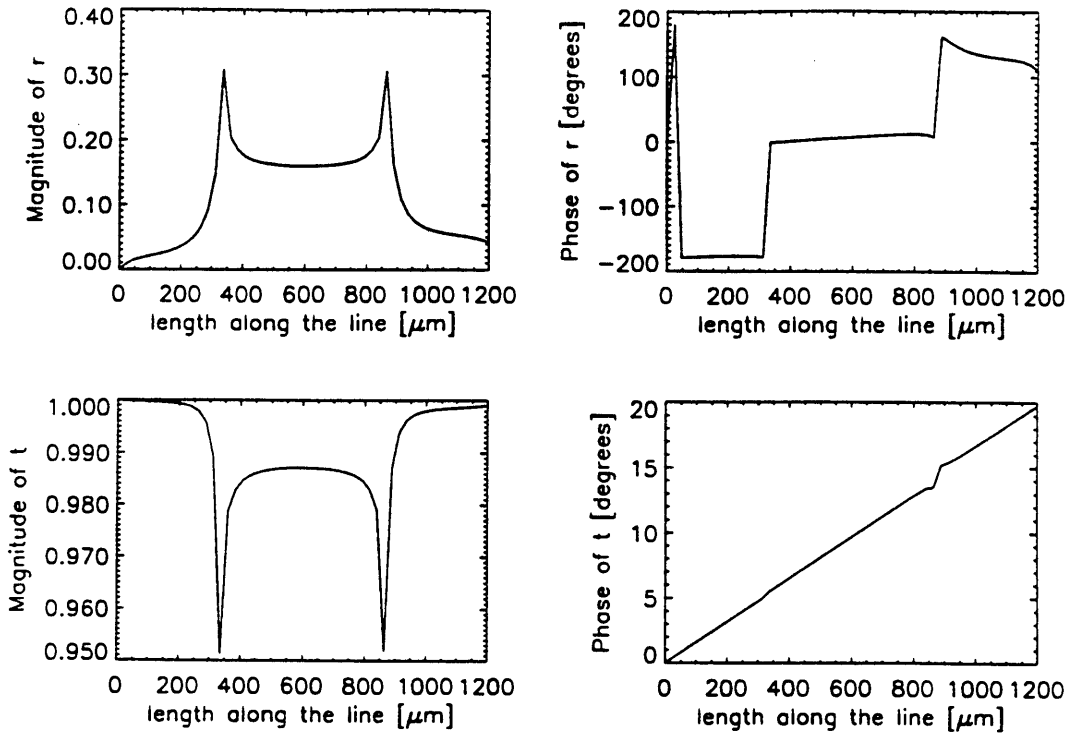

Figure 4.4. Magnitude and phase of reflection and transmission S-parameters along the line at $f = 5\,\mathrm{GHz}$.

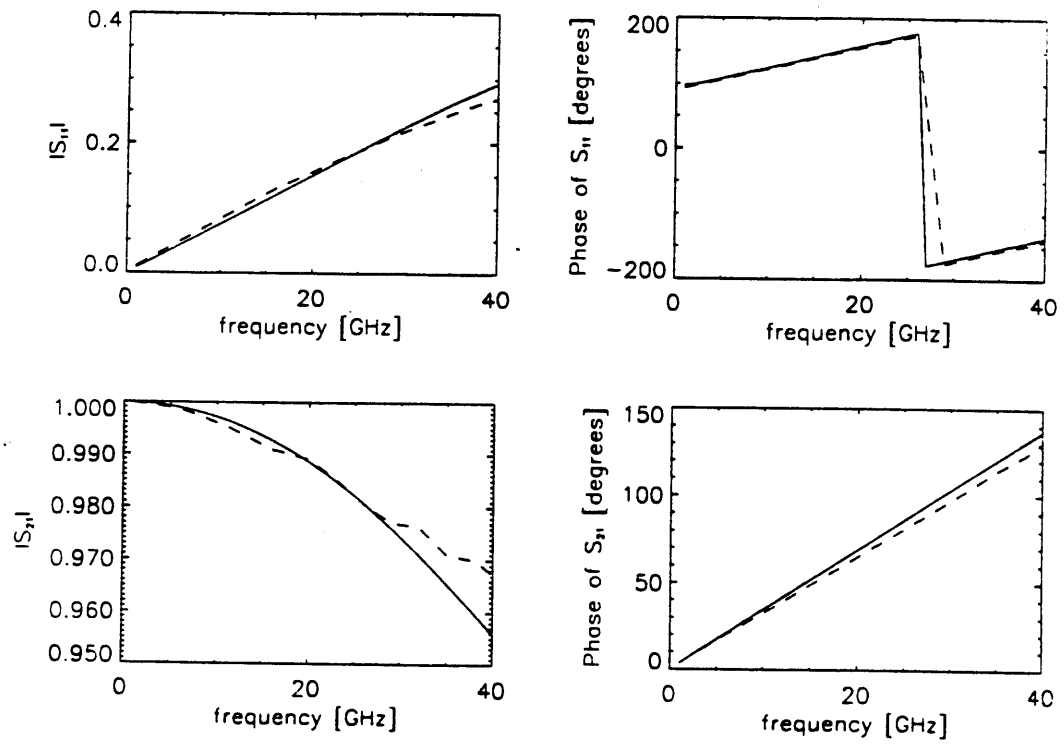

Figure 4.5. Magnitudes and phases of S_{11} and S_{21}. The quasi-static results are shown in solid line, while PMESH full-wave analysis results are shown with a dashed line.

In both the quasi-static and full-wave algorithms, most of the computation time is used for inverting the Greens function matrix. For the full-wave technique, a matrix inversion is needed for every frequency point. For the quasi-static approach only one matrix inversion is needed, and the time needed to calculate the S-parameters for each additional frequency is negligible. Therefore, with approximately the same number of cells for the two approaches, the time needed to compute S-parameters for a wide frequency range (e.g. from 0 to 40 GHz) using quasi-static approach should be comparable to the time needed to compute one frequency point using the full-wave program. Also, the time domain response (using FFT) can be obtained easily.

4.2 Other Test Structures

Other test structures we have analyzed include: a CPW structure with several sections of the same impedance ($50\,\Omega$ on GaAs) but different geometry, Figure 4.6 and a CPW bend ($56\,\Omega$ on GaAs), Figure 4.7. For each of these structures, the charge distributions, capacitance per unit length, impedance, reflection and transmission S-parameters along the propagation coordinate and S-parameters were found. Examples of these results were shown in Figures 4.8 and Figure 4.9. Figure 4.8 shows the capacitance per unit length and impedance as a function of the propagation coordinate for the test structure shown in Figure 4.6. We can compare these results with the characteristic impedance of the CPW line without discontinuities using Equation (4.1). The values for the impedance, from Figure 4.8 away from the discontinuity are about $50\,\Omega$ for the connecting lines and about $45\,\Omega$ for the inner part, which is less than $50\,\Omega$ because the length of the inner part is comparable with the effective wavelength. Figure 4.9 shows the calculated S-parameters for the test

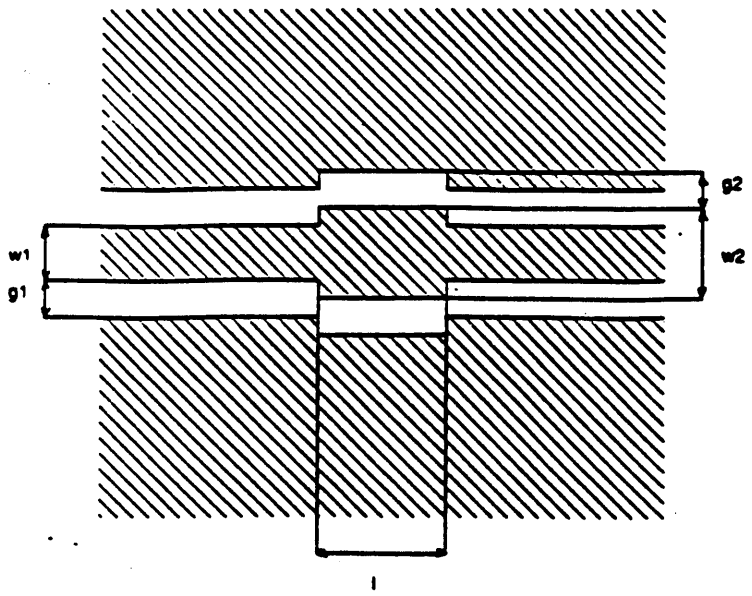

Figure 4.6. A CPW test structure, where $g_1 = 56\,\mu$m, $w_1 = 80\,\mu$m, $g_2 = 86\,\mu$m, $w_2 = 124\,\mu$m and $l = 335\,\mu$m and all transmission line sections have the same impedance ($50\,\Omega$ on GaAs).

structure shown in Figure 4.7.

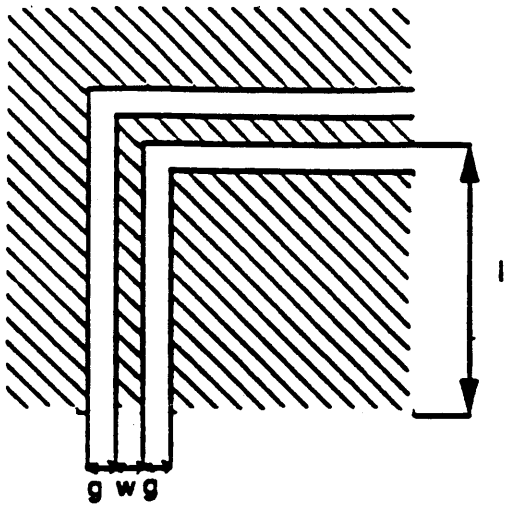

Figure 4.7. A CPW 56 Ω test structure on GaAs, where $g = 80\,\mu$m, $w = 80\,\mu$m and $l = 160\,\mu$m.

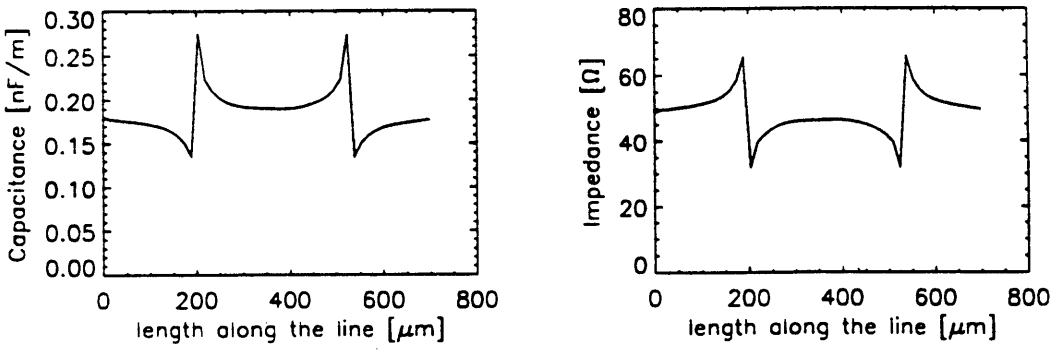

Figure 4.8. The capacitance per unit length and impedance as a function of the propagating coordinate for the test structure shown in Figure 4.6.

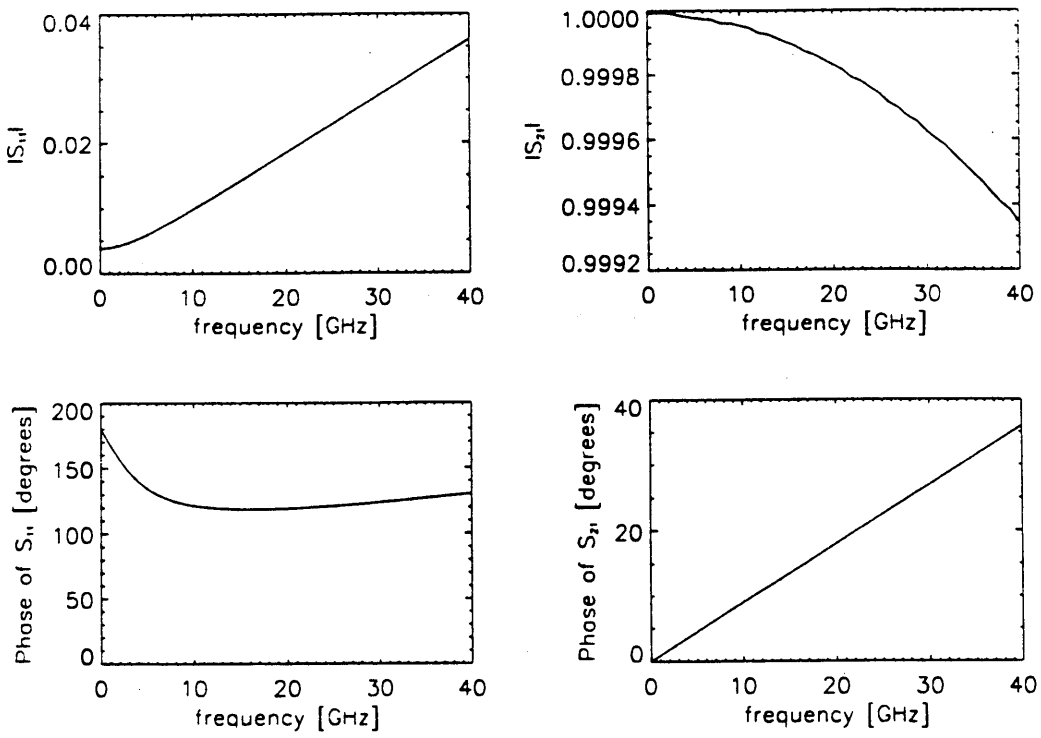

Figure 4.9. The calculated S-parameters for the 56 Ω bend on GaAs, from Figure 4.7.

CHAPTER 5

EXPERIMENTAL VERIFICATION

5.1 Electrooptic Sampling Measurements

Direct electrooptic sampling measurements of circuits on GaAs substrates can provide a relative 2-D potential distribution given by

$$V_{eos}(x,z) = const \cdot \int \vec{E}(x,y,z) \cdot \vec{dl}, \tag{5.1}$$

where $\vec{dl}$ is tangential to the path of the probe beam. For the configuration shown in Figure 5.1, the resulting potential distribution is proportional to the potential difference between the two surfaces. For sufficiently thick substrates, one could assume the bottom surface is an equipotential. For such a case, the line integral in the Equation (5.1) should give the relative spatial (in x and z) variation of the potential distribution on the top surface [22]. The measured potential distribution is therefore identical to within a constant factor, which will be assumed to be zero, to the transmission line voltage defined in the quasi-TEM analysis. These measurements can be used to either directly verify the accuracy of the static potential distributions used in the analysis, or as input to the algorithm and subsequently used to compute transmission line parameters and S-parameters.

Hence, electrooptic sampling measurements of the local quasi-static field distributions combined with the program developed in this paper provides technique for calculating the S-parameters. To explore the feasibility of this technique we have taken electrooptic sampling measurements on the structure

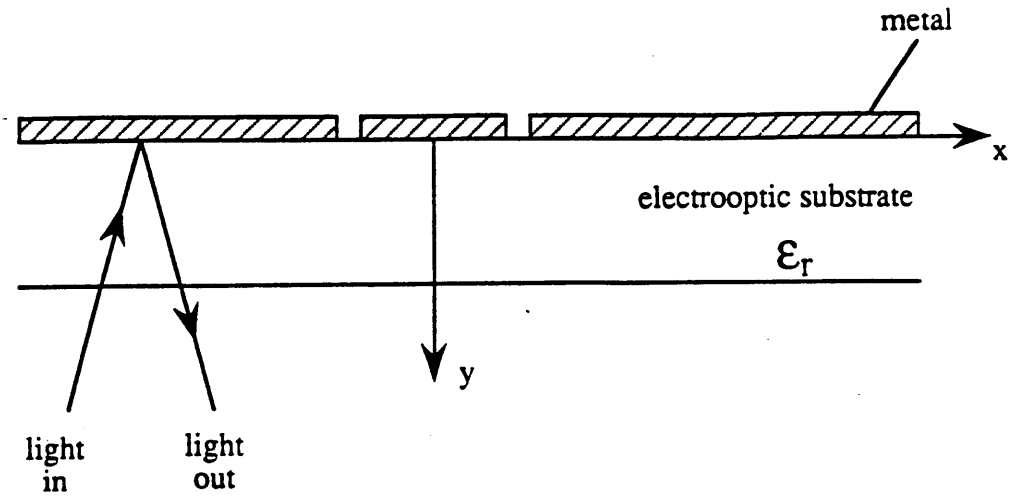

Figure 5.1. Optical sampling shown in a transverse cross section of a CPW line.

analysed in the previous section.

The test structure from Figure 4.1 was fabricated on a 400 μm thick GaAs substrate. The circuit was tested using a wafer probe station built for electrooptic probing [7]. Figure 5.2 (a) shows the measured 2-D potential distribution For comparison, Figure 5.2 (b) shows the static potential distribution computed from the charge distribution shown in Figure 4.2. Aside from some local anomalies in the measured result, that can be attributed to surface defects on the wafer, and fewer grid points in the theoretical data, the comparison is quite good.

To check whether we can accurately determine the charge distribution from the measured potential distribution, and therefore compute the equivalent transmission line parameters from the measurements, we first analyzed the 1-D cross section problem. Figure 5.3 shows the measured and computed voltage distribution in one cross-section. The comparison is good, except at the points close to the edges of the center conductor. The large spikes are most likely due

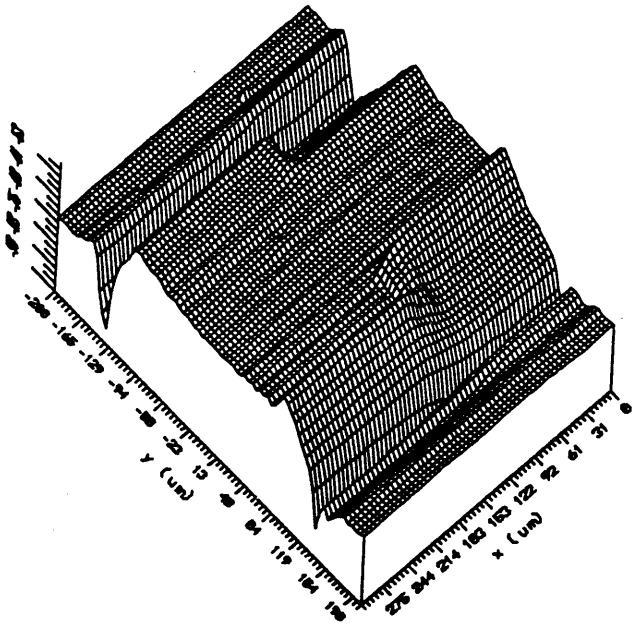

(b)

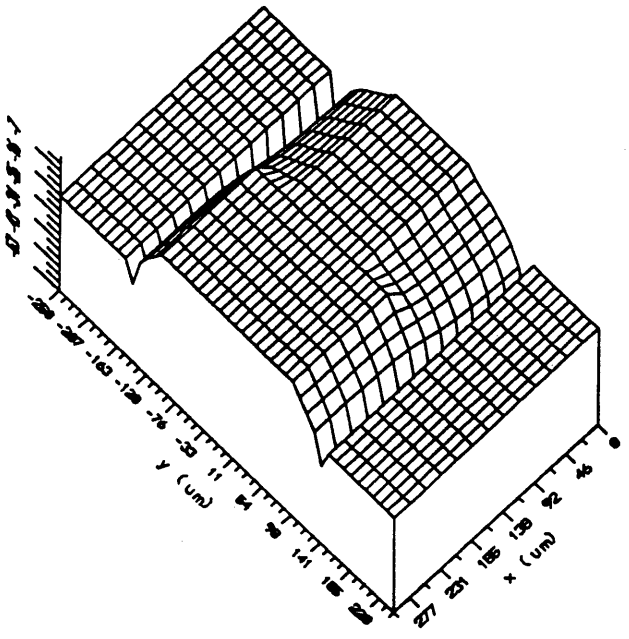

(a)

Figure 5.2: Measured (a) and computed (b) 2-D voltage distribution.

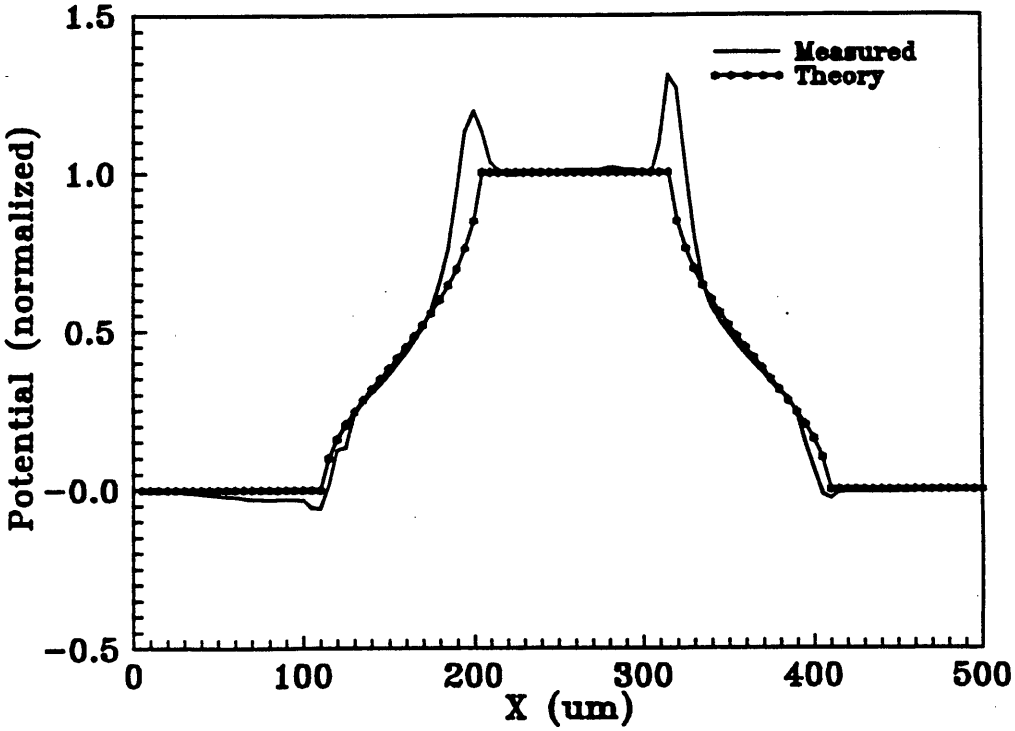

Figure 5.3. Comparison of voltage distributions, in a transverse cross section, from measurements and theory.

to optical diffraction effects at the edges. The slightly negative values on the ground plane can be attributed to the finite substrate thickness [22]. By first eliminating the spikes in the measured potential, we computed the 2-D charge distribution from the measured data. Figure 5.4 shows the comparison of the charge distributions, for one cross-section, calculated from the measured and assumed potentials. The small ripples in the measured result are due to fluctuations in the measured conductor potentials. However, it is the total charge on the center conductor that determines the local impedance. Therefore, the accuracy of the "measured" impedance should be sufficient to obtain accurate S-parameter results.

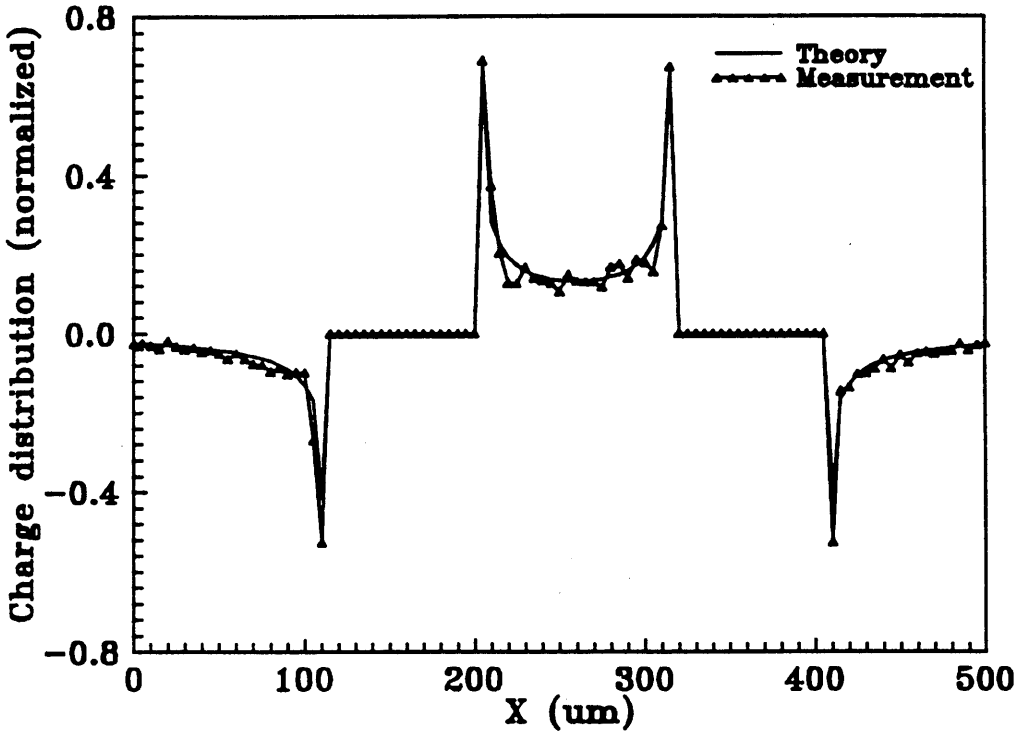

Figure 5.4. Comparison of charge distributions, in a transverse cross section, calculated from measured and assumed voltage distributions.

5.2 Network Analyzer Measurements

Additional measurements were performed on the fabricated structure from Figure 4.1, using the HP8510 network analyzer and the NIST Deembed software [23]. Figure 5.5 shows comparison between theoretical and measured S-parameters. Results for S_{11} from measurment and theory differ at most 3 dB up to 40 GHz. For S_{21} note that the scale goes from 0 dB to -0.4 dB and the results show some disagreement that is due to the noise in measured result. Figure 5.6 shows results for:

(a) effective dielectric constant versus frequency. The measured result is about 7, which verifies the assumption that $\epsilon_{eff} = \frac{\epsilon_s+1}{2}$, since $\epsilon_s = 13$ for GaAs;

(b) attenuation versus frequency, which is less than 1 dB/cm, except for a spike at 32 GHz, probably due to coupling between TRL standards on the wafer; and

(c) characteristic impedance of a straight line versus frequency, which is about 52 Ω for frequencies between 1 and 40 GHz. Deembed program uses different definition for the impedance than it was used in this thesis. Therefore, their characteristic impedance increases as the effective dielectric constant is increased, while if one uses our definition it would be opposite.

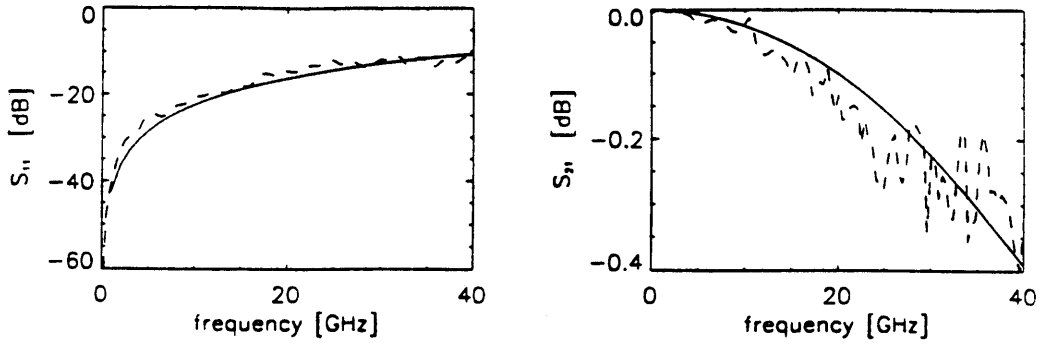

Figure 5.5. S-parameters for test structure from Figure 4.1 comparison between theoretical (solid line) and network analyzer (dashed line) measurements.

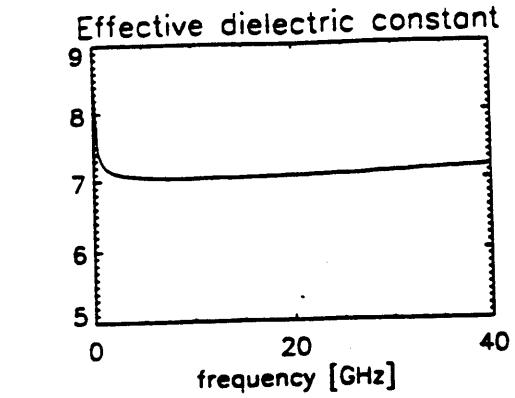

(a)

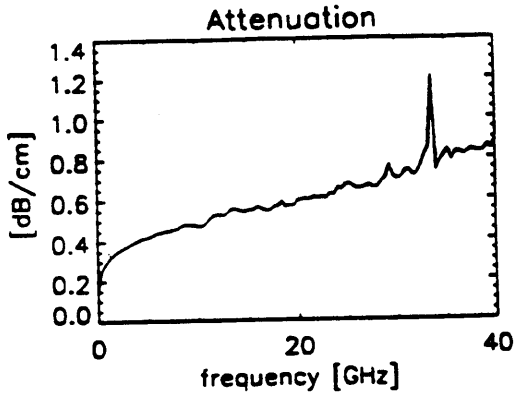

(b)

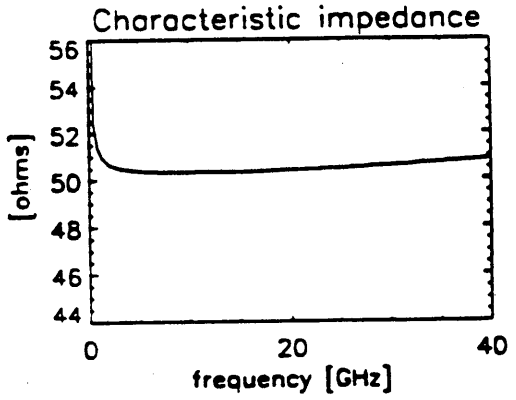

(c)

Figure 5.6. Results for test structure from Figure 4.1, using on-wafer probing and NIST Deembed software: (a) effective dielectric constant, (b) attenuation and (c) characteristic impedance versus frequency.

CHAPTER 6

CONCLUSION AND FUTURE DIRECTIONS

In this work, we presented a quasi-static technique for analyzing two-dimensional discontinuities in two-port CPW circuits. However, there is no fundamental limitation on the number of ports. For multiport circuits the static part is the same as described, but the dynamic part will involve using a set of coupled matrix Riccati equations [24].

The examples discussed in this thesis assumed planar 2-D circuits. In CPW circuits, airbridges need to be included in order to suppress the radiative slot mode. These airbridges are 3-D structures and in order to model them the Green's function from equation (2.21) need to be used and the method has to be applied in 3-D.

In conclusion, we have presented a new technique for obtaining the frequency dependent scattering parameters of waveguide discontinuities. Using a quasi-static field analysis, the discontinuity is transformed into an equivalent nonuniform transmission line. The transmission line parameters are computed from the static charge distribution. The scattering parameters are found by analyzing the propagation along this line. The approximation used, neglecting the longitudinal field components on the equivalent transmission line, is the same as used for the quasi-TEM analysis of uniform inhomogeneous transmission lines. The error in the transverse field on the equivalent transmission line are of second order in the expansion coefficient ($\alpha = k\omega$). The longitudinal

field components, proportional to the first order in α, are neglected. The technique is substantially faster than full-wave techniques and for sufficiently small line dimensions compared to the wavelength, the accuracy should rival that of full-wave techniques.

Several application of this technique have been presented. First, the technique is applied to a double step-in-impedance discontinuity, computing the S-parameters up to 40 GHz. Results are compared with the results from network analyzer measurements and from a full-wave analysis of the same structure. By combining the technique with the direct electrooptic sampling technique, it is shown that one can obtain local S-parameters from measurement of the local 2-D potential distribution. While we have only considered passive structures here, it is our hope that the technique can be extended to include active devices. This would then provide a technique for finding the parasitic reactances due to the device electrode geometry.

BIBLIOGRAPHY

[1] R.N.Simons and G.E.Ponchak, "Modeling of some coplanar waveguide discontinuities," *IEEE Trans. Microwave Theory Tech., vol. 36,* pp. 1796-1803, 1988.

[2] M.Naghed and I.Wolff, "Equivalent capacitances of coplanar waveguide discontinuities and interdigitated capacitors using a three dimensional finite difference method," *IEEE Trans. Microwave Theory Tech., vol. 38,* pp. 1808-1815, 1990.

[3] R.Brömme and R.H.Jansen, "Systematic investigation of coplanar waveguide MIC/MMIC structures using a unified strip/slot 3-D electromagnetic simulator," *IEEE MTT Digest,* pp. 1081-1084, 1991.

[4] C.W. Kuo and T. Itoh, "Characterization of shielded coplanar type transmission line junction discontinuities incorporating the finite metalization thickness effect," *IEEE Trans. Microwave Theory Tech., vol. 40,* pp. 73-80, 1992.

[5] A.R.Djordjevic, T.K.Sarkar and Z.Maricevic, " Evaluation of excess inductance of microstrip discontinuity," *Radio Sience, vol. 26,* pp. 565-570, 1991.

[6] K.J. Weingarten, M.J.W. Rodwell and D.M. Bloom, "Picosecond optical sampling of GaAs integrated circuits," *IEEE J. of Quantum Electron., vol. QE-24,* pp. 198-220, 1988.

[7] D.R. Hjelme, M.J.Yadlowsky and A.R. Mickelson, "Two-dimensional mapping of the microwave potential on MMICs using electrooptic sampling," *submitted to IEEE Trans. Microwave Theory Tech.,* May 1992.

[8] C.C. Lin and L.A. Segel, **Mathematics Applied to Deterministic Problems in the Natural Sciences,** Macmillan Publishing, New York, 1974.

[9] G.K. Grünberger, V. Keine, H.H. Meinke, "Longitudinal field components and frequency-dependent phase velocity in the microstrip transmission line," *Electron. Lett., vol. 6,* pp. 683-685, 1970.

[10] A.F. dos Santos and J.P. Figanier, "The method of series expansion in frequency domain applied to multidielectric transmission lines," *IEEE Trans. Microwave Theory Tech., vol. MTT-23,* pp. 753-756, 1975.

[11] E.F.Kuester, D.C.Chang and L.Lewin, " Frequency-dependent definitions of microstrip characteristic impedance," *Digest of the Int. URSI Symp. Electromagnetic Waves (Munich),* Aug. 26-29, p. 335 B/1, 1980.

[12] J.R.Brews, " Characteristic impedance of microstrip lines," *IEEE Trans. on Microwave Theory Tech., vol. MTT-35,* pp. 30-34, 1987.

[13] L.C.Shen and J.A.Kong, **Applied Electromagnetism,** PSW Publishers, pp. 356-358, Boston, MA, 1987.

[14] P.S.Weitzman, J.M.Dunn and A.R.Mickelson, "An efficient numerical algorithm for the calculation of the electrical properties of coplanar electrodes in the presence of a buffer layer," accepted for publication, *Journal of Quantum Electronics.*

[15] W.P. Press, B.P. Flannery, S.A. Teukolsky and W.T. Vetterling, **Numerical Recipes in Pascal,** Cambridge University Press, Cambridge, 1989.

[16] R.F.Harrington, **Field Computation by Moment Methods,** Malabar, Florida, Robert E. Krieger Publishing Company, 1968.

[17] R.L. Burden and J.D. Faires, **Numerical Analysis,** PWS-Kent Publishing Company, Boston, 1989.

[18] W.C. Chew, **Waves and Fields in Inhomogeneous Media,** Von Nostrand Reinhold, 1990.

[19] S.Barkeshli and P.H.Pathak, " On the Dyadic Green's function," *IEEE Trans. on Microwave Theory Tech., vol. 40,* pp.140-142, January 1992.

[20] K.C. Gupta, R. Garg and R.Chadha, **Computer-Aided Design of Microwave Circuits,** Artech House, pp. 25-46 and 67-69, 1981.

[21] S.Petrakos. **Electromagnetic Modeling of Coplanar Waveguide Discontinuities,** Masters Thesis, University of Colorado at Boulder, 1991.

[22] J.L. Freeman, D.M. Bloom, S.R. Jefferies, and B.A. Auld, " Accuracy of electro-optic measurements of coplanar waveguide transmission lines," *Appl. Phys. Lett., vol. 53,* pp. 7-9, 1988.

[23] R.B.Marks and D.F.Williams, **Characteristic Impedance Determination Using Propagation Constant Measurements,** National Institute of Standards and Technology, Boulder, Colorado, March 1991.

[24] A.R. Mickelson, **Electromagnetic Wave Propagation in Almost Periodic Media,** Antenna Laboratory Report No. 90, California Institute of Technology.